Ultraviolet metasurface-assisted photoacoustic microscopy with great enhancement in DOF for fast histology imaging

Wei Song [a],[*], Changkui Guo [a], Yuting Zhao [a], Ya-chao Wang [b], Siwei Zhu [c], Changjun Min [a],[*], Xiaocong Yuan [a],[d],[**]

[a] *Nanophotonics Research Center, Shenzhen Key Laboratory of Micro-Scale Optical Information Technology, Institute of Microscale Optoelectronics & State Key Laboratory of Radio Frequency Heterogeneous, Shenzhen University, Shenzhen 518060, China*
[b] *Depart of Neurosurgery, The First Affiliated Hospital of Shenzhen University, Shenzhen Second People's Hospital, Shenzhen 518060, China*
[c] *The Institute of Translational Medicine, Tianjin Union Medical Center of Nankai University, Tianjin 300121, China*
[d] *Research Center for Humanoid Sensing, Zhejiang Laboratory, Hangzhou 311100, China*

ARTICLE INFO

ABSTRACT

Pathology interpretations of tissue rely on the gold standard of histology imaging, potentially hampering timely access to critical information for diagnosis and management of neoplasms because of tedious sample preparations. Slide-free capture of cell nuclei in unprocessed specimens without staining is preferable; however, inevitable irregular surfaces in fresh tissues results in limitations. An ultraviolet metasurface with the ability to generate an ultraviolet optical focus maintaining < 1.1-μm in lateral resolution and ~290 μm in depth of field (DOF) is proposed for fast, high resolution, label-free photoacoustic histological imaging of unprocessed tissues with uneven surfaces. Microanatomical characteristics of the cell nuclei can be observed, as demonstrated by the mouse brain samples that were cut by hand and a ~3 × 3-mm^2 field of view was imaged in ~27 min. Therefore, ultraviolet metasurface-assisted photoacoustic microscopy is anticipated to benefit intraoperative pathological assessments and basic scientific research by alleviating laborious tissue preparations.

1. Introduction

Histology examination of tissues remains the gold standard for the diagnosis and management of various diseases, and it is also a foundational technique in preclinical and scientific research [1]. However, routine histology examination requires time-consuming preparations of slides including tissue fixation, embedding, sectioning, and staining. The pathological assessment of tissue specimens involves a significant delay ranging from hours to days, which imposes difficulties on intraoperative cancer margin identification during tumor surgeries or degrades the efficiency on lesion differentiation in the basic research. Alternatively, frozen sections offer fast histological analysis [2]; however, the histology slide quality is often compromised because freezing the sample may cause artifacts in the edematous and soft tissue [3]. Additionally, it is difficult to apply the frozen section approach to hard tissues (e.g., cortical bone and calcified tumors) because of the ossification [4]. The incorporation of frozen section histology into surgical practices suffers from unsatisfactory interpretation of the tissue specimens such as breast or bone.

To achieve accurate histology analysis with rapid imaging acquisition, efforts have been directed towards revolutionizing biomedical imaging techniques. Optical microscopy methods, such as confocal microscopy [5], wide-field microscopy [6], multiphoton microscopy [7], and microscopy with ultraviolet surface excitation (MUSE) [8], acquire images of biological tissues at cellular and even subcellular levels. Fluorescence-based approaches, relying on the administration of fluorescent agents on the specimens for sufficient imaging contrast [5,8], still require complicated staining procedures. Label-free visualization of morphological characterizations is assessed by autofluorescence contrast of endogenous chromophores; however, the inherently weak autofluorescence signals restrict the applications of multiphoton microscopy to only translucent tissues [7]. Rapid histological imaging of tissues is realized using computational microscopy without sectioning and staining [6], which otherwise involves very complicated image

---

processing because the cell nucleus generates imaging contrast opposite that of hematoxylin labeling used in standard histology analysis. Optical coherence tomography (OCT) has micrometer-level resolution along the depth direction. However, the nuclear specificity is usually absent because of its optical scattering-based imaging contrast such that it is not acceptable in clinical pathology examinations that employ hematoxylin and eosin (H&E) staining [9]. Stimulated Raman scattering (SRS) microscopy has label-free imaging capability [10]; however, it's small depth of field (DOF) deteriorates the imaging quality of unprocessed specimens with uneven surfaces.

Photoacoustic microscopy (PAM) is an emerging technology that detects acoustic waves (i.e., photoacoustic signals) caused by the transient thermoelastic expansion of biomolecules arising from the absorption of laser energy, and it can optically measure the absorption properties of intrinsic biomolecules directly [11,12]. Because of the strong optical absorption of DNA/RNA at the wavelength of 266 nm, the cell nucleus is specifically highlighted without exogenous contrast agents by an ultraviolet (UV)-PAM system, and hence, histology-like images are displayed with the same contrast as hematoxylin labeling in the conventional histology examinations [13–16]. The depth-resolved ability encoded in the time-domain photoacoustic signal provides multilayered imaging of tissue samples, which circumvents physical sectioning in standard histology imaging or axial scanning for reconstructing z-stacked images [5–7,10].

Microscopic observations with subcellular resolution are essential for histological examinations of tissue specimens; as a result, PAM necessitates optical focusing of the UV excitation laser using an objective with high numerical aperture (NA) [13–16]. However, because those are optical microscopy techniques [5–10], the trade-off between the DOF and spatial resolution (i.e., a higher spatial resolution corresponding to a shorter DOF) compromises the image quality because of out-of-focus blurring when using unprocessed thick tissues with uneven surfaces. For example, UV-PAM has a typical DOF of ~20 μm [13–16], much smaller than the height fluctuation of the tissue surface (>100 μm) [16, 17]. Therefore, for surgical resection specimens, a substantially rough surface fundamentally poses a challenge for rapid, slide-free histology imaging in practical intraoperative pathology examinations because severe out-of-focus blurring ultimately hinders the histology interpretations of the images. According to the surface profile, axially translating the sample enables PAM to consistently project its optical focus onto the sample surface, thus realizing high-quality imaging of the cell nuclei [17]. However, determining and updating the z-scanning contour trajectory during the raster scanning creates serious loads of data processing and system control, and pixels can still fall out of the DOF because of inadequate mechanical movement of the z motor. Alternatively, wavefront engineering by digitally modulating the complex fields of a photoacoustic illumination laser can elongate focus along the depth direction, enabling nearly invariant diffraction-limited lateral resolution within an extended depth range, thus accommodating the surface irregularity [18,19]. Because of the physical limitations, current commercial devices, such as a spatial light modulator (SLM) and digital micromirror device (DMD) [18–20], fail to manipulate the UV wavefront that is indispensable for label-free photoacoustic histology-like imaging of cell nuclei. Bessel-mode beam can be generated by inserting an axicon into the illumination path, significantly elongating the focal depth [21–23]. However, the imaging quality possibly compromises because of both low efficiency of the Bessel beam and complicated system configuration due to additional components in the optical path.

By designing a planar array of subwavelength electromagnetic structures to tailor the amplitude, phase, or polarization of the incident light, an optical metasurface emulates conventional optical functionalities using a refractive, birefringent, or diffractive optical component, including a lens, waveplate, or hologram [24–27]. Compared with SLM or DMD [18–20], metasurfaces with nanostructured dielectric elements [28–30], such as aluminum nitride or hafnium oxide, are capable of operating at very high frequencies up to the deep UV range (i.e., ≤ 280

nm wavelength), demonstrating the capabilities of precisely manipulating UV light focusing, routing, and multiplexing with low loss. Therefore, we designed a high performance dielectric metasurface for sculpturing the optical focus of UV illumination via wavefront shaping of the incident laser beam, which enabled a PAM system with consistent diffraction-limited lateral resolution (< 1.1 μm) along a remarkably extended depth range (~290 μm), significantly surpassing the traditional UV-PAM that has a focal depth of ~20 μm [13–17]. Without additional acquisition and/or processing times, or complex arrangements of optical and acoustic components [6,7,17], PAM incorporating a UV metasurface with its optical absorption contrast of label-free highlighting cell nuclei and acoustically-defined depth resolving ability [11–17] reveals subcellular microanatomic characteristics at the rough surfaces of unprocessed tissues. Multiple advantages of a UV metasurface-assisted PAM system allow for fast histological imaging of freshly harvested tissues by avoiding complex sectioning and staining procedures; as a result, there is great promise for streamlining standard-of-care histological examinations for intraoperative pathological diagnosis and management of neoplasms and other diseases.

2. Results and discussion

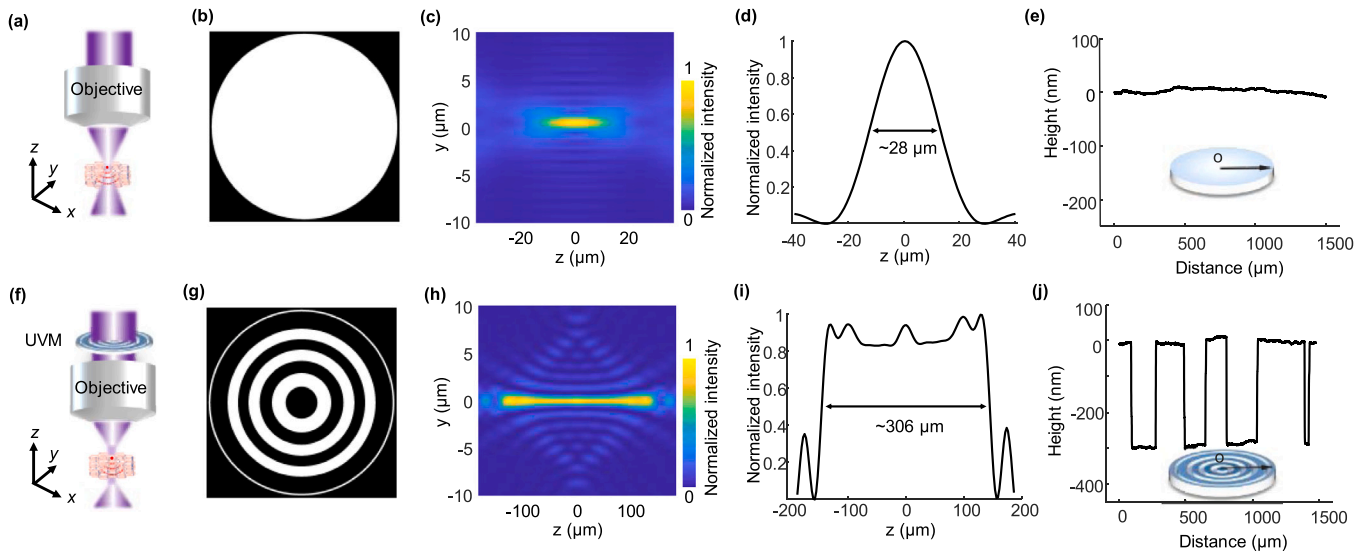### 2.1. A UV metasurface for engineering photoacoustic illumination

In traditional UV-PAM systems [13–18], an optical objective (NA = 0.13) is usually used for focusing the UV excitation laser, producing a diffraction-limited focus spot on the samples (Figs. 1a-d). With a clear back aperture of the objective (Figs. 1a and b), the lateral resolution is theoretically ~1.10 μm according to the full-width-at-half-maximum (FWHM) value of the light intensity distribution at the focus spot along the transverse direction (Fig. 1c), which is only maintained within a very short depth (~28 μm in Fig. 1d). When imaging the unprocessed tissue specimens with rough surfaces, the image blurs because the cell nuclei are away from the optical focus and the histology examinations are deteriorated [17,18].

To produce an optical focal field with a longer DOF, an extended Nijboer–Zernike theory is exploited for engineering the objective's pupil function (Note 1; Supporting Information) [31,32]. According to the one-to-one correspondence between the Zernike polynomials ($Z_{2k}(\rho, \theta)$ that create the pupil field) and the functions ($V_{2k}(r, z)$ that produce the electric field in the objective's focal region) [31], we can directly engineer the intensity distribution of the electric field ($E(r, \varphi, z)$) at the focus from the complex Zernike coefficients ($\beta_{2k}(\rho, \theta)$), where (ρ, θ) represent polar coordinates and (r, φ, z) represent cylindrical coordinates, respectively. Considering a circularly symmetric focal field, the desired electric field intensity in the focal region is determined by the precalculated functions $V_{2k}(r, z)$ [31], expressed as $|E(r, \varphi, z)|^2 \propto \left| \sum_{k=0}^{N} \beta_{2k} V_{2k}(r, z) \right|^2$. Thus, the corresponding pupil function ($E_0(\rho, \theta)$) can be immediately derived from $E_0(\rho, \theta) = \sum_{k=0}^{N} \beta_{2k} Z_{2k}(\rho, \theta)$. Because the extended Nijboer–Zernike theory only computes a limited number of Zernike coefficients that comprise pupil function for generating a predesigned focal field, the operations are significantly faster than the diffraction integral approaches [33].

Despite the successful applications in the light modulation within the visible–infrared range [18–20], commercial devices, such as DMD and SLM, cannot operate at the UV spectrum yet and they are inadequate for label-free imaging of cell nuclei. A customized UV metasurface with appropriate phase patterns is proposed for generating the pupil function (Figs. 1f and g) that allows for manipulating the electric field intensity in the focal region (Fig. 1h) by wavefront engineering of the incident light beam. Compared with the focus spot of a conventional Gaussian beam in the simulations (Fig. 1c and d), the metasurface significantly elongates the DOF by ~11 folds (Figs. 1h and i) while maintaining an excellent lateral resolution of < 1.1 μm within the elongated focus length.

Fig. 1. Principle of a UV metasurface for sculpturing optical focus. (a) and (f) Schematic diagrams of focusing photoacoustic illumination without and with a UV metasurface, respectively. (b) A clear back aperture of an objective by positioning a glass substrate that produces an optical diffraction-limited light field (c). (d) Light intensity distribution along the optical axis of the focus spot. (e) Measured height profile of the glass substrate that is positioned before the objective when performing the traditional PAM imaging. (g) Phase pattern of the UV metasurface in which the phase is π and 0 in the black and white regions, respectively. (h) An extended DOF by assigning the UV metasurface onto the objective's back aperture. (i) Light intensity distribution along the optical axis. (j) Measured height profiles of the UV metasurface producing the predesigned phase distribution in (g). UVM: UV metasurface.

Concurrently, the beam features a nearly uniform axial intensity (~5.3%) within the whole focal region in which the uniformity is defined as the ratio of the difference between the maximal intensity and minimal intensity to the sum of the two values. The combined capabilities of an extended focal depth, micrometer-scale lateral resolution, and uniform axial intensity distribution realized by the metasurface enables the UV-PAM system for imaging unprocessed tissues with rough surfaces.
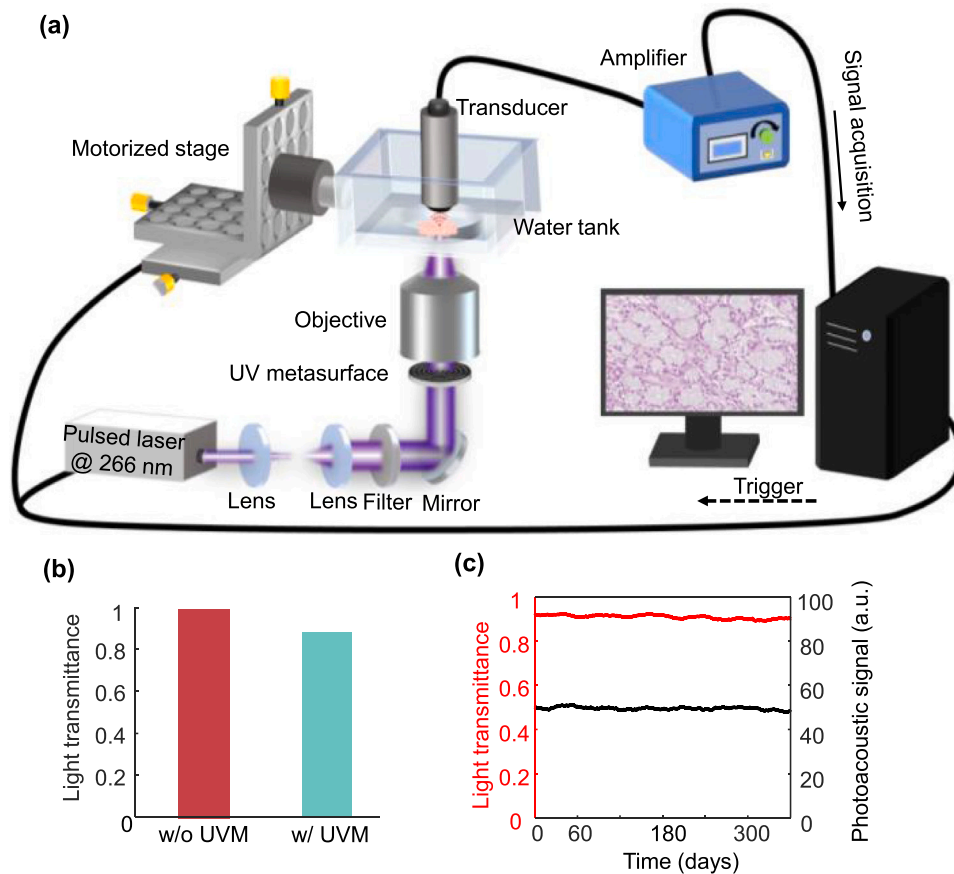
Fig. 2. (a) Schematic diagram of the UV metasurface-assisted PAM system. (b) Measured light transmittance with and without the UV metasurface. (c) Long-term monitoring of both light transmittance and photoacoustic signal amplitude using the UV metasurface. UVM: UV metasurface.

Taking advantage of well-established nanomanufacturing technologies of direct laser writing (DLW) in combination with the reactive ion etching (RIE) process [34,35], fabrications of UV metasurfaces (Fig. S1a-e, Supporting Information) are accomplished on a substrate of double-side-polished, UV-grade fused silica. Alternant annulus grooves with only two heights of the UV-grade fused silica are created with the RIE process, producing the predesigned phase pattern (i.e., phase at 0 or π). According to the 266 nm wavelength photoacoustic illumination and refractive index of the fused silica ($n = 1.49$), the height of the annulus groove with respect to the fused silica surface is easily determined by converting into the desired phases (Fig. 1j). Simply fabricating the UV metasurface permits a very high yield and less time consumption. Moreover, the metasurface has excellent optical transparency that is critical for high quality photoacoustic histology imaging, surpassing the nano-optical elements that suffer from relatively large light energy loss in the UV spectral region [29,30]. Although the UV metasurface has only two step phases (Figs. 1g and j), the extended DOF in photoacoustic illumination is adequate for high quality histology imaging (refer to details in Figs. 3-7).

2.2. UV metasurface-assisted PAM

By placing the compact UV metasurface (1.0 mm thickness and 3.0 mm diameter; Fig. S1f, Supporting Information) before the objective, the UV-PAM system is readily converted to an extended DOF (Fig. 2a) [36], avoiding complicated reconfigurations of the optical, mechanical, and electronic components. Unprocessed thick specimens with rough surfaces can be directly imaged using the UV metasurface-assisted PAM, enabling a rapid pathological diagnosis. The light power is ~91% of the incident photoacoustic illumination

(Fig. 2b), demonstrating the metasurface's slight optical attenuation that is created by the nanomanufacturing processing of the UV-transparent fused silica without high optical loss materials. Long-term monitoring of both light transmittance and photoacoustic excitation after the UV metasurface (Fig. 2c) indicates that its excellent performance persists at least one year (Note 2, Supporting Information).

The system's lateral resolution was evaluated by imaging ~200-nm diameter carbon nanospheres (Fig. 3a), where the insets show the representative images captured without (labeled by a red box) and with (labeled by a blue box) the UV metasurface, respectively. According to the FWHM values of the Gaussian fitting of the photoacoustic amplitudes across the nanoparticles, the lateral resolution in the two imaging modalities is estimated at ~1.16 μm ± 0.17 μm and ~1.13 μm ± 0.16 μm, respectively, both of which are in accordance with the theoretical values. To measure the DOF, the nanoparticles are moved along the optical axis, and the images sequentially acquired at each axial location determine the corresponding lateral resolution at different depths (Fig. 3b). Without the UV metasurface, the lateral resolution deteriorates quickly as the sample moves away from its original position, indicating a very short focal depth of ~21 μm. As expected, the integration of the UV metasurface improves the DOF (~290 μm) by more than an order of magnitude in which the lateral resolution is consistently finer than ~1.2 μm. Without a complicated system reconfiguration or imaging processing [6,17], the cell nuclei of the unprocessed tissues with irregular surfaces are sufficiently resolved using a UV metasurface. The two photoacoustic excitation modalities share the same axial (depth) resolution of ~62 μm (Figs. 3c and d), predominantly determined by the bandwidth of the customized ultrasonic transducer (central frequency: ~22 MHz, −6 dB bandwidth: 81%) [37]. The customized transducer maintains > 90% of the maximum acoustic signal within a
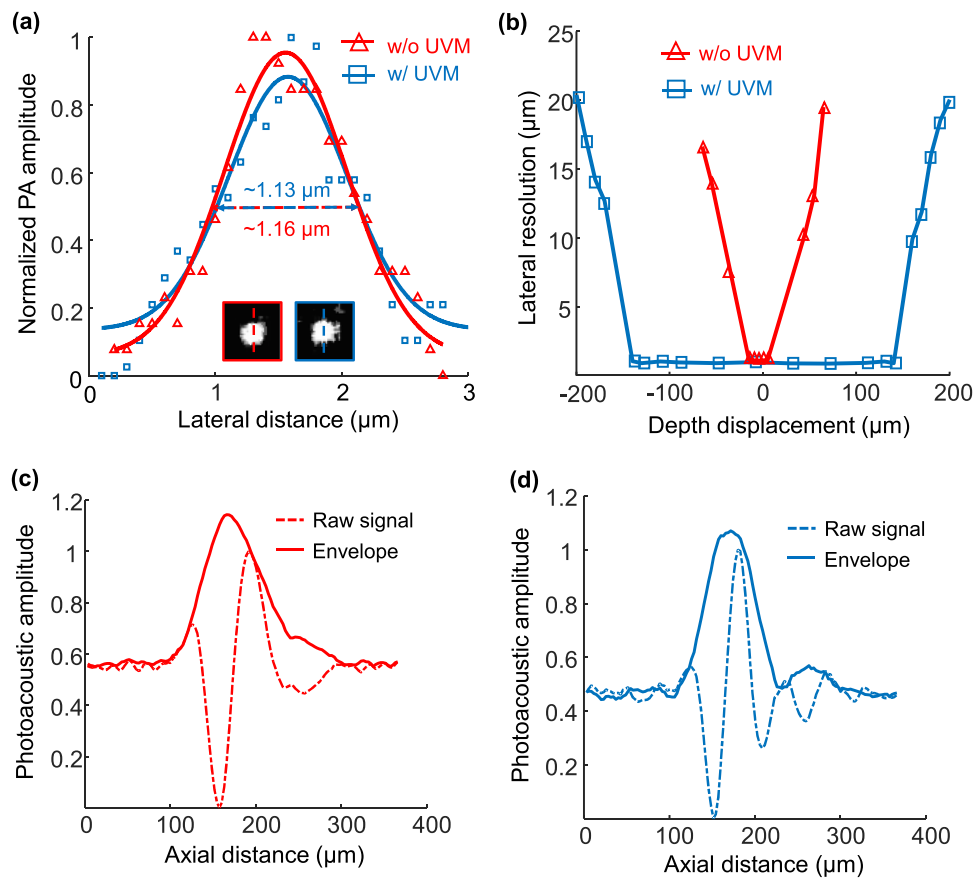
Fig. 3. Characterization of the UV metasurface-assisted PAM system. (a) Determination of the lateral resolution; the insets show the representative images of nanoparticles captured by the system without and with the UV metasurface, respectively. (b) Axial distributions of the lateral resolution indicate the focal depths of the two systems. (c, d) The system's depth resolution without and with a UV metasurface. UVM: UV metasurface.

depth range of ~360 μm (Fig. S2, Supporting Information), which is much greater than the UV metasurface-determined DOF and thus ensures a uniform ultrasound detection sensitivity at different axial positions. By aligning the optical and acoustic response region, a faithful PAM imaging acquisition can be accessed within the optical DOF.

2.3. Volumetric imaging of a phantom

To demonstrate the volumetric imaging capability of our PAM system incorporating a UV metasurface, a phantom made of spatially distributed tungsten filaments (~10 μm in diameter; Fig. S3, Supporting Information) was captured, as shown in Fig. 4. Only three tungsten filaments were observed in the conventional PAM system (Fig. 4a-c), whereas a large portion of filaments were missing because of their out-of-focus location. From the B-scan view (Fig. 4b) that corresponds with the position highlighted by the white dotted line in Fig. 4a, the three filaments (labeled by white arrows in Fig. 4b) had a maximum axial distance of ~30 μm, suggesting correspondence with the DOF determined by the objective's NA and the excitation laser wavelength. Alternatively, the UV metasurface-assisted PAM system visualizes more filaments (Figs. 4 d-f) than the conventional system. Other than the three filaments with very close distance (labeled by the white arrows in Fig. 4e), the B-scan view (Fig. 4e) that corresponds to the position highlighted by the white dotted line in Fig. 4d reveals well-resolved features of the phantom throughout a depth range of ~300 μm. This is attributed to a significantly extended focal depth arising from the modulation to the optical field by the UV metasurface (Fig. 3b). The filament cluster remains resolvable in three-dimensional (3D) space because of the UV metasurface (Fig. 3f; Movie S2, Supporting Information), and the conventional PAM system cannot otherwise image the filaments at the distance from the focal plane (Fig. 3c; Movie S1, Supporting Information).

Supplementary material related to this article can be found online at doi:10.1016/j.pacs.2023.100525.

Supplementary material related to this article can be found online at doi:10.1016/j.pacs.2023.100525.

2.4. Histology imaging of brain slices using UV metasurface-assisted PAM

To demonstrate label-free histology imaging of the UV metasurface-assisted PAM system, mouse brain slices (~7.0 μm thickness) were imaged, as shown in Fig. 5. Images from three adjacent slices were captured to compare the histology imaging acquired by the standard H&E staining (Fig. 5a), the conventional PAM system (Fig. 5b), and UV metasurface-assisted PAM system (Fig. 5c). For PAM imaging (Figs. 5b and c), no staining procedure was performed, and the photoacoustic images were presented by taking a maximum amplitude projection (MAP) of each A-line along the depth direction because of the thinner slice than the system's axial resolution. It took about 27 min to acquire the brain slice image with a field of view (FOV) of ~3.0 mm (x) × 3.0 mm (y) when setting ~1.0-μm step size. The image acquired using the UV metasurface-assisted PAM system resembled both the standard H&E-stained image and conventional PAM image. Magnified views (Figs. 5 d-f) of the regions marked by the dashed boxes in Figs. 5a-c show a nearly identical appearance of the cell nuclei (noted by the light blue arrows in Figs. 5d-f) with comparably high resolution and contrast. The structural similarity index measurement (SSIM) [39], which is a multiplicative combination of the luminance term, the contrast term, and the structural term, was calculated to be ~0.82 for the cell nuclei of the H&E-stained image (Fig. 5d) and UV metasurface-assisted PAM image (Fig. 5f). The imperfect spatial match mainly arises from the different tissue slices and possibly deformed anatomic structures during the
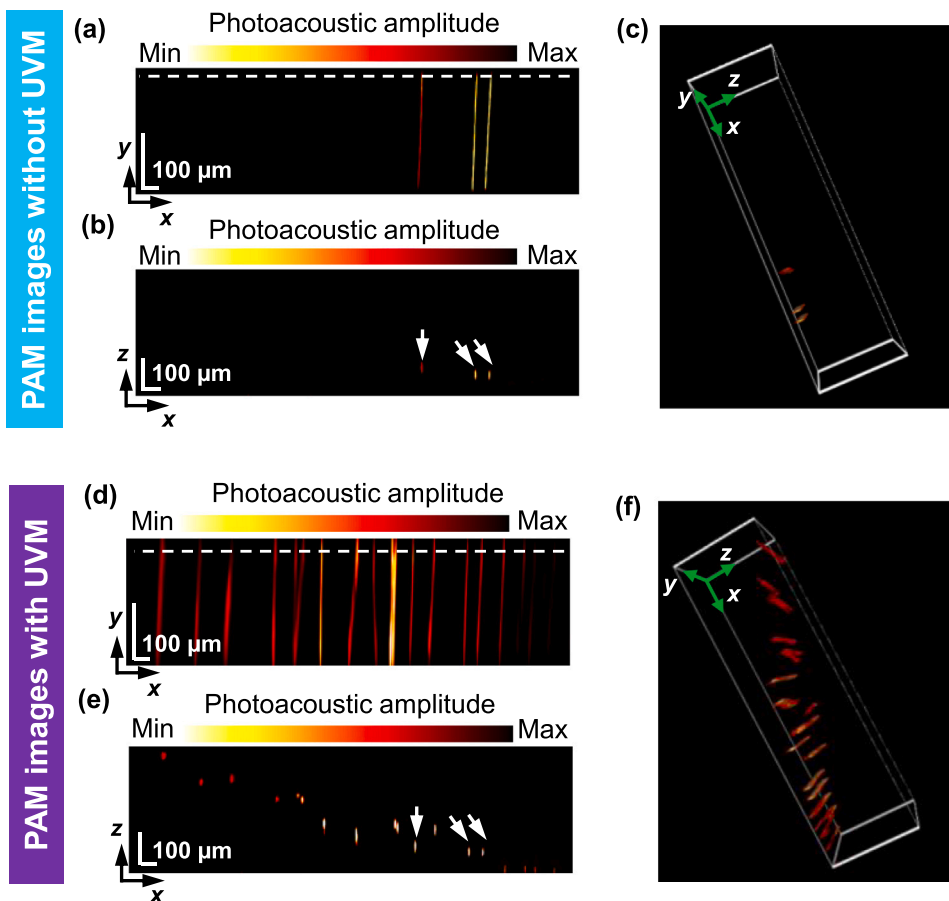

Fig. 4. Volumetric imaging of a phantom. (a) Photoacoustic image of the phantom without the UV metasurface in which the visualizations are displayed in the maximum-amplitude-projection (MAP) view, (b) B-scan image, and (c) three-dimensional view. (d) Photoacoustic image of the phantom using the UV metasurface in which the visualizations are displayed in the MAP view, (e) B-scan image, and (f) three-dimensional view. The white dotted lines in (a) and (c) indicate the positions of the B-scan images in (b) and (d), respectively.
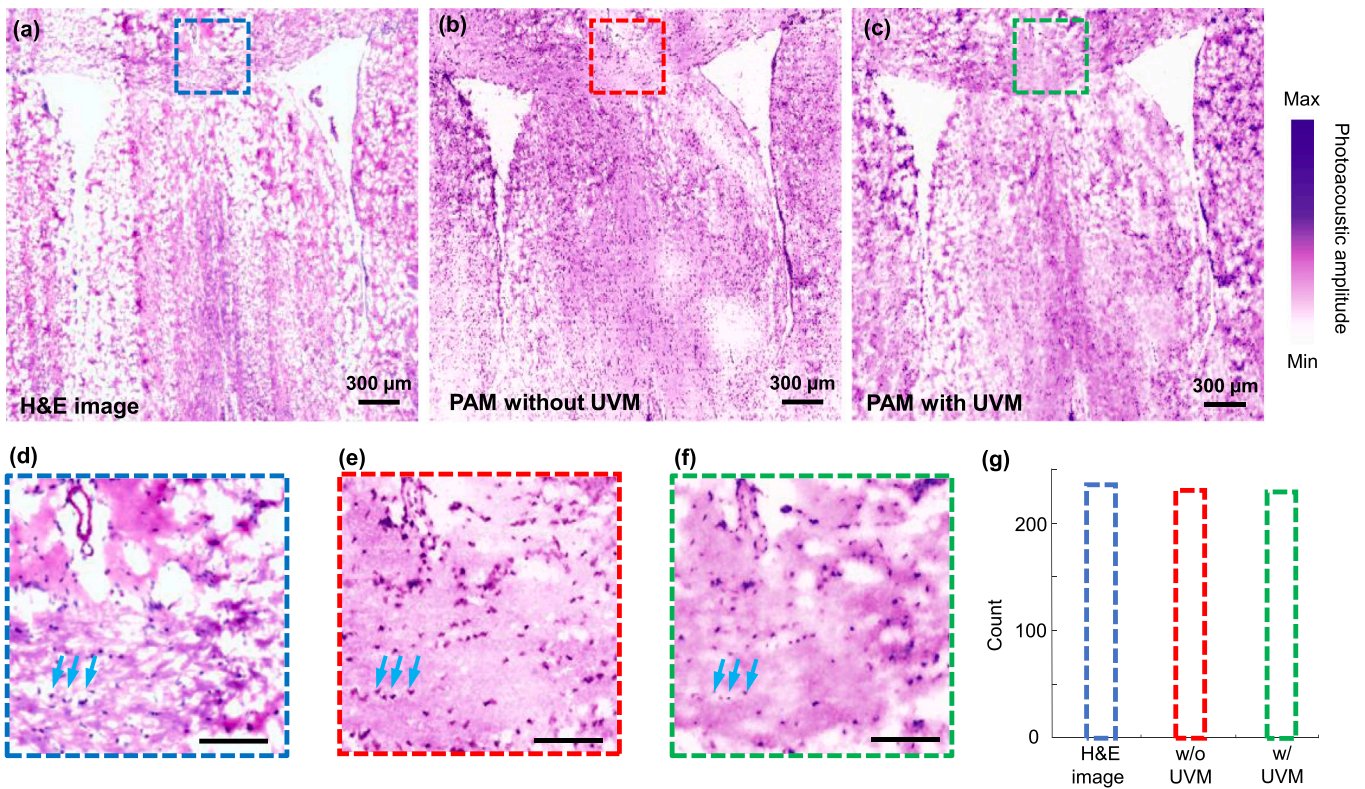
Fig. 5. Photoacoustic histology imaging of mouse brain slices. (a-c) Standard H&E staining, conventional PAM, and UV metasurface-assisted PAM images where the slices are from the adjacent tissue layers. (d-f) Magnified views from the corresponding regions marked by dashed boxes in (a-c), respectively. (g) The number of cell nuclei identified in the three images (d-e). Scale bars in (d-f): 100 μm. UVM: UV metasurface.
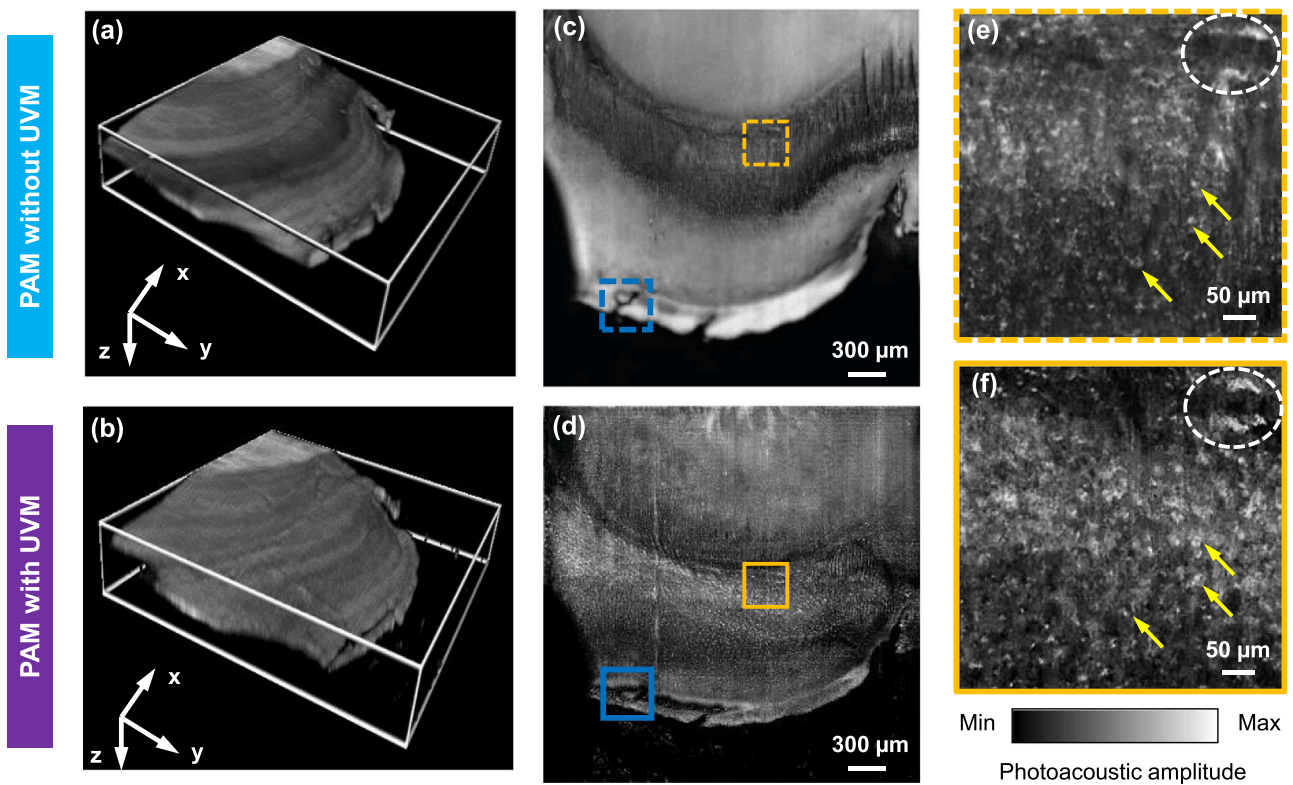

Fig. 6. Photoacoustic histology imaging of hand-cut, thick brain samples. (a) and (b) Volumetric images captured by the conventional PAM and UV metasurface-assisted PAM, respectively, corresponding to the MAP images in (c) and (d). (e) and (f) Magnified images of the corresponding positions marked by yellow dashed and solid boxes in (c) and (d), respectively. UVM: UV metasurface.

sample processing procedures in the H&E staining [13,36]. Because the two slices were obtained from adjacent layers and prepared with the same processing procedures, the SSIM increases to ~0.86 between the conventional PAM image and UV metasurface-assisted PAM image (Figs. 5e and f). Building upon the excellent lateral resolution with the UV metasurface, the number of cell nuclei was easily identified as 227 in the UV metasurface-assisted PAM image (Fig. 5g), which is similar to those from the H&E-stained image (235) and conventional PAM image (228). On the basis of the clear visualization of the cell nuclei, by incorporating a UV metasurface, our PAM system is capable of acquiring microanatomic features as both standard H&E-stained images and label-free photoacoustic histology imaging methods; therefore, accurate histological examinations can be assessed using the UV metasurface-assisted PAM system.

2.5. UV metasurface-assisted PAM imaging of unprocessed brain samples

Furthermore, we performed slide-free histology imaging of thick tissues using the UV metasurface-assisted PAM, where hand-cut fresh samples (~1.0 mm in thickness) were extracted from an excised mouse brain without any other tissue processing. Photoacoustic volumetric imaging was implemented by setting the FOV to 3.0 mm (x) × 3.0 mm (y) (Fig. 6), which required approximately 27 min to capture an image comprising 3000 pixels × 3000 pixels. For comparison, conventional PAM imaging and UV metasurface-assisted PAM imaging were implemented in the same sample sequentially. As expected, both imaging modalities (Figs. 6a and b) delineate rough surface in the volumetric images because of unprocessed tissue sample from the manual cut processing.

Using the conventional PAM (as displayed in volumetric view in Fig. 6a and MAP view in Fig. 6c, respectively), the histology image appears blurry in a large proportion of the image. The microstructures were identified in a confined region (indicated by yellow dashed boxes in 6c) that axially coincides with the DOF of the conventional PAM, whereas the cell nuclei were barely resolved at other depths that locate out-of-focus areas (Fig. 6c; Movie 3, Supporting Information). By contrast, incorporating the UV metasurface provides a clear identification of microanatomic structures in the same FOV (Figs. 6b and d).

Because of the extended focal depth from the UV metasurface, a consistent subcellular resolution across the total imaging area enables well-resolved visualization of the cell nuclei (Fig. 6d; Movie 4, Supporting Information), effectively mitigating the difficulties from obvious surface irregularity of the unprocessed sample. In the regions located at the optical focus (Figs. 6e and f), the histology images in both imaging modalities exhibited microstructures of the cell nuclei, as identified by yellow arrows and white dotted ellipses. Compared with the conventional PAM image (Fig. 6e), additional features (Fig. 6f) were observed to correspond to the cell nuclei or other microanatomic structures from neighboring depths [16] that were captured with the increased DOF in the UV metasurface assisted PAM.

Supplementary material related to this article can be found online at doi:10.1016/j.pacs.2023.100525.

Supplementary material related to this article can be found online at doi:10.1016/j.pacs.2023.100525.

We compare the magnified histology images in Figs. 7a and b, which are from the corresponding positions marked by the blue dashed and solid boxes in Figs. 6c and d, respectively. Blurring profiles were only observed when the imaging area was away from the focal plane of the conventional PAM system (as illustrated in MAP view in Fig. 7a). However, numerous discrete cell nuclei were clearly distinguished in the same area (as illustrated in MAP view in Fig. 7b) because the focal depth was greater in the UV metasurface. By digitally sectioning the raw dataset according to the acoustic time of flight, depth-resolved images are reconstructed as shown in Z_1 and Z_2 views (Figs. 7a and b). At both layers (axial distance of ~78 μm between Z_1 and Z_2), many discrete cell nuclei (pointed out by green arrows) were clearly visualized with sufficient contrast by the UV metasurface-assisted PAM. Unfortunately, the conventional PAM fails to identify the cell nuclei in the region in which the microanatomic structure is barely recognizable. As illustrated in Figs. 7c and d, the UV metasurface allows for imaging with much clear boundary and gap between the microstructures (marked by red solid line at Z_1 view and yellow solid line at Z_2 view, respectively, in Fig. 7b), compared with the images captured by the conventional PAM, suggesting that both resolution and contrast are superior with the UV metasurface-assisted PAM. A detailed comparison of the photoacoustic histology images from the two imaging modalities indicates the
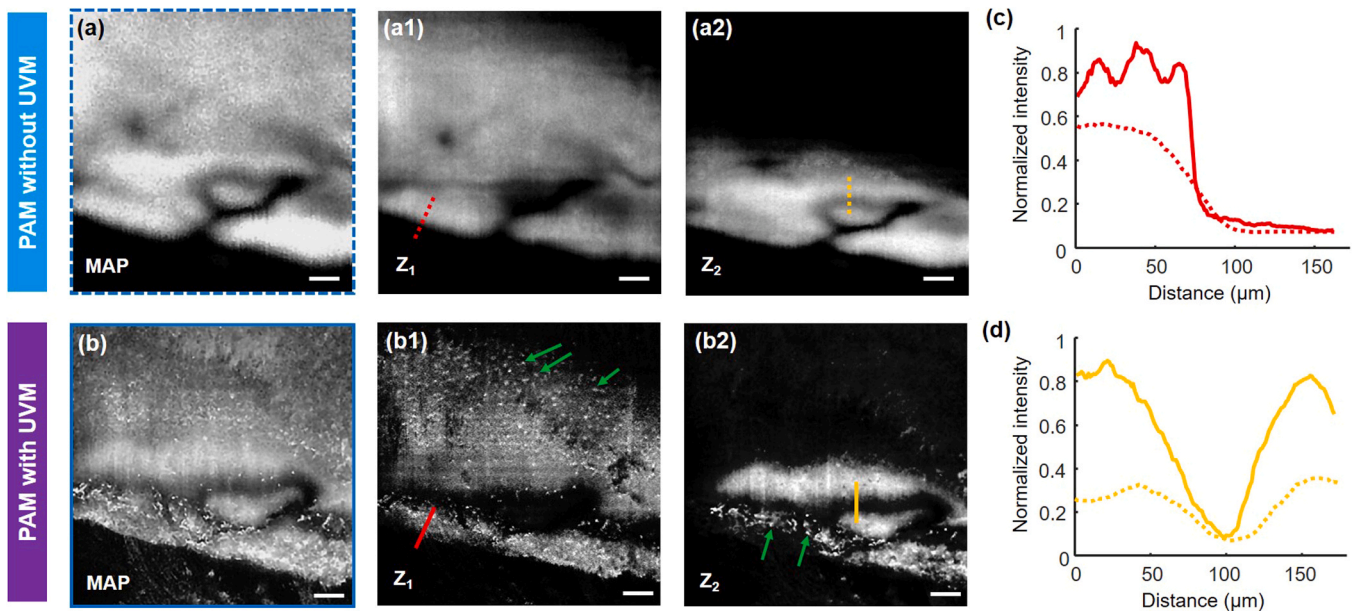
Fig. 7. (a) and (b) Magnified images from the corresponding positions marked by blue dashed and solid boxes in Fig. 6(c) and (d), respectively, in which the MAP views and depth-resolved views (labeled by Z_1 and Z_2) demonstrate the disparity of both resolution and contrast between the two imaging modalities. (c) and (d) Comparison of sample boundaries (labeled by red dashed and solid lines at Z_1 layer in (a1) and (b1), respectively) and gaps (labeled by yellow dashed and solid lines at Z_2 layer in (a2) and (b2), respectively) of the images. Scale bars in (a, b): 100 μm. UVM: UV metasurface.

favorable capabilities of resolving the microstructure of the irregular sample surfaces achieved by simply inserting a compact UV metasurface in the photoacoustic illumination path. It is medically meaningful to precisely determine the fine lesions of the unprocessed specimens to enhance intraoperative decision-making [1–5].

3. Conclusion

We proposed a UV metasurface for wavefront shaping of photoacoustic excitation laser at a 266-nm wavelength that enables the PAM system with an elongated focal depth (~290 μm) while maintaining subcellular lateral resolution (<1.1 μm) within the DOF by positioning the compact metasurface (3.0 mm in diameter, 1.0 mm in thickness) at the objective's back aperture. Such nano-optic element circumvents complicated system reconfigurations (e.g., microtomy sectioning or contour scanning) that require expensive hardware [16,17]. Label-free highlighting of the cell nuclei of the brain tissue slices from the UV metasurface-assisted PAM was validated by the standard H&E-stained image (Fig. 5). Moreover, the UV metasurface allows for label-free, slide-free visualizations of the hand-cut tissue specimens with irregular surfaces (Figs. 6 and 7), in which a high-quality image of the cell nuclei across the whole FOV is captured in approximately 27 min (a 3 × 3-mm^2 area with a 1.0-μm step size). Without a UV metasurface, the conventional PAM had a very short focal depth and failed to identify the finer structures of unprocessed tissues with rough surfaces because a large portion image was out of focus. Recently, Cao et al. proposed diffractive optical element-based UV-PAM with an extended needle-shaped focus (~1.2-μm lateral resolution and ~200-μm DOF) for histology-like imaging of fresh slide-free organs in which four lithography steps achieved 16 heights that were employed for device manufacture [40]. In comparison, we designed a UV metasurface based on an extended Nijboer–Zernike theory [31,32], allowing for straightforward fabrication via the highly efficient generation of only two heights while realizing ~290-μm DOF at a < 1.1-μm lateral resolution.

For preclinical research and clinical translation, further improvements in the UV metasurface-assisted PAM are required for practical histopathological examination of tissue samples. Intraoperative assessment relies on fast imaging acquisition over a sufficient FOV, which usually suffers from the physical difficulties from both UV laser repetition rate and mechanical raster scanning. High speed imaging can be realized by introducing a hybrid scanning mechanism that applies the optical scanning of a galvanometer mirror with mechanical scanning [41,42], thus producing subcellular visualization of the samples within a few of minutes of a typical biopsy. Additionally, the implementation of deep learning approaches permits increasing the PAM scanning step size to realize under-sampled histology imaging reconstruction [43,44]. The system has poor optical sectioning capability along the depth direction, predominantly determined by the limited ultrasonic bandwidth of the piezoelectric transducer [37]. To clearly distinguish anatomic features in three-dimensions, photoacoustic volumetric imaging requires better axial resolution that is comparable to the thickness of the standard histology slice (~7.0 μm). Enhancing the ultrasonic frequency response bandwidth by exploiting optical sensing technologies [45–47], such as micro-ring resonance detectors, silicon-on-insulator resonators, or optical surface wave sensors, could overcome the drawbacks of conventional piezoelectric transducers. Thus, 3D photoacoustic histology imaging can be reconstructed with micrometer-scale resolution capability along the depth direction. In current PAMs, photoacoustic excitation and ultrasonic detection are on opposite sides of the targets, which may create difficulties for imaging complicated anatomic sites with a larger thickness. By applying a transparent ultrasonic detector or ring transducer [17,46], the PAM system could operate in reflection mode to accommodate more preclinical and clinical applications.

In summary, with the ability to control the photoacoustic illumination laser at a 266-nm wavelength, a UV metasurface, which is readily fabricated using the well-established nanomanufacturing technologies

of DLW in combination with the RIE process, offers the prospects of performing fast histology imaging of unprocessed thick tissue samples by improving PAM with an increased DOF while maintaining subcellular lateral resolution. High quality images of the cell nuclei from freshly harvested tissue samples with rough surfaces were obtained without time consuming sectioning and staining typically required in conventional histopathological processes. Therefore, by further improving the imaging performances, our UV metasurface assisted-PAM system may be an ideal intraoperative assessment tool during cancer resection surgeries.

4. Materials and methods

4.1. Design and fabrication of UV metasurfaces

The fabrication processes of the UV metasurfaces mainly entail spin coating photoresist, DLW exposure, RIE following development, and photoresist rinsing, as schematically illustrated in Fig. S1 (Supporting Information). Double-side-polished UV-grade fused silica (~1.0 mm in thickness; Daheng Optics, China) is the substrate (refractive index of 1.49). One droplet of the photoresist (AZ1500, IMM, Texas, USA) is placed on the glass substrate and then soft baked at 100 °C for 30 min (Fig. S1a; Supporting Information). According to the predesigned phase patterns based on the extended Nijboer–Zernike theory [31], the DLW exposure (Fig. S1b; Supporting Information), operating at a 405-nm wavelength and ~300 mW irradiation power, was performed for direct patterning on the photoresist using a direct write lithography system (Heidelberg DWL66 +, Germany). Following the development (Fig. S1c; Supporting Information), the fused silica is etched via RIE (PlasmaPro 80 RIE, Oxford Instruments Plasma Technology, UK), creating grooves on the substrate (Fig. S1d; Supporting Information) that have an average height difference (*h*) of ~273 nm (Dektak XT, Bruker, Germany). Considering the photoacoustic illumination wavelength ($\lambda_0 = 266$ nm) and the fused silica's refractive index ($n_g = 1.49$), the relative phase difference ($\Delta\varphi$) between the substrate surface and groove was derived from $\Delta\varphi = 2\pi(n_g-1)h/\lambda_0$, which approximates to π and agrees well with the predesigned phase patterns (Fig. 1 g). After photoresist removal by plasma degluing machine (Fig. S1e; Supporting Information), the UV metasurface (~3.0 mm in diameter) is complete with multiple concentric rings, as shown in the optical photograph (Fig. S1f; Supporting Information).

4.2. UV metasurface-assisted PAM

The UV metasurface is incorporated into PAM for engineering the optical wavefront of the photoacoustic excitation light to achieve an increased DOF, as illustrated in Fig. 2a. The photoacoustic illumination uses a nanosecond UV pulsed laser (266 nm wavelength; Picolo 1, InnoLas Laser GmbH) as the laser source. After passing through a pair of lenses and spatially filtering using a 25-μm-diameter pinhole, the expanded incident beam, which is adjusted to be slightly wider than 3.0 mm, overfills the UV metasurface's active area (Fig. 1j). An objective (NA: 0.13, 3.0-mm diameter back aperture; U-13X-LC, Newport) is used to focus the photoacoustic excitation laser onto the specimens. When performing UV metasurface-assisted PAM imaging, the metasurface is conveniently positioned onto the objective's back aperture, which is replaced using a clean glass substrate (Fig. 1e) for acquiring the conventional PAM images. The brain tissue specimens are placed in a water tank that is fabricated with a layer of membrane underneath for optical and acoustic transparency. The tank is mounted on a scanning stage (MS-2000, ASI, Oregon, USA). A customized water-immersed ultrasonic transducer is used to detect the photoacoustic signals, which are amplified by an amplifier (5073PR, Olympus NDT Inc., TX, USA) and then digitized by a data acquisition card (ATS9350, Alazar Technologies Inc., Pointe-Claire, QC, Canada). A LabVIEW-programmed interconnect card (PCIe-6353, National Instruments, Austin, TX) is used for triggering

the UV laser firing and data acquisition, as well as controlling the raster scanning.

4.3. Brain specimen preparation and photoacoustic imaging

To validate the PAM imaging, brain slices from the mice were imaged. After euthanasia, the mice brains are cut into slices with a thickness of ~7.0 μm (CryoStar™ NX50 Cryostat, Thermo Fisher Scientific, Waltham, MA, USA). Three adjacent slices were extracted for the H&E staining image, conventional PAM image, and UV metasurface-assisted PAM image to consider nearly identical anatomic structures. The slice was stained with standard H&E staining, and then images were captured under bright field optical microscopy. For PAM imaging, the slices are transferred onto a quartz coverslip that served as a transparent optical window for UV illumination.

To demonstrate the capability of imaging unprocessed tissue specimens using the UV metasurface-assisted PAM system, fresh brain tissue from the euthanized mice were cut into thicker samples (~1.0 mm) to serve as imaging targets. Immediately after harvest, the thick samples were gently sandwiched using a piece of membrane and then immersed into deionized water. Such procedures created an optically- and acoustically transparent platform for the immobilization of brain tissue while avoiding possible interference of the tissue structures. We implemented the imaging acquisitions to the same tissue regions by sequentially activating the conventional PAM and UV metasurface-assisted PAM. When performing the conventional PAM imaging, the photoacoustic illumination energy on the sample surface was measured to be ~10 nJ per pulse. Because of the reduced light fluence of the focus from the UV metasurface, the energy increases to ~18 nJ per pulse to ensure similar signal-to-noise ratio as conventional PAM imaging, which is still within the American National Standards Institute safety standard (3.0 mJ/cm^2) [38].

For imaging reconstructions, each depth-resolved photoacoustic image (A-line) was generated from one single laser pulse by recording the time course of the photoacoustic signal without signal averaging, which formed the 3D images via 2D raster scanning of the samples. Because the slices were much thinner than the PAM system's depth resolution, the photoacoustic MAP images of the thin mouse brain slices were reconstructed. All procedures were performed according to local government and approved by the Ethics Committee of Shenzhen University (Protocol Number: AEWC-2019001).

Declaration of Competing Interest

The authors declare no conflicts of interest.

Data Availability

The data that support the findings of this study are available from the corresponding authors upon reasonable request.

Acknowledgements

References

[1] F. Fleming, A.D. Hill, E. Mc Dermott, A. O'Doherty, N. O'Higgins, C. Quinn, Intraoperative margin assessment and re-excision rate in breast conserving surgery, Eur. J. Surg. Oncol. 30 (2004) 233–237.

[2] V. Rastogi, N. Puri, S. Arora, G. Kaur, L. Yadav, R. Sharma, Artefacts: a diagnostic dilemma - a review, J. Clin. Diagn. Res 7 (2013) 2408–2413.

[3] S.R. Shi, C. Liu, L. Pootrakul, L. Tang, A. Young, R. Chen, R.J. Cote, C.R. Taylor, Evaluation of the value of frozen tissue section used as "gold standard" for immunohistochemistry, Am. J. Clin. Pathol. 129 (2008) 358–366.

[4] S.A. Taqi, S.A. Sami, L.B. Sami, S.A. Zaki, A review of artifacts in histopathology, J. Oral. Maxillofac. Pathol. 22 (2018) 279.

[5] J. Dobbs, S. Krishnamurthy, M. Kyrish, A.P. Benveniste, W. Yang, R. Richards-Kortum, Confocal fluorescence microscopy for rapid evaluation of invasive tumor cellularity of inflammatory breast carcinoma core needle biopsies, Breast Cancer Res. Treat. 149 (2015) 303–310.

[6] Y. Zhang, L. Kang, I. Wong, W. Dai, X. Li, R. Chan, M. Hsin, T. Wong, High-throughput, label-free and slide-free histological imaging by computational microscopy and unsupervised learning, Adv. Sci. 9 (2022), e2102358.

[7] X. Li, H. Li, X. He, T. Chen, X. Xia, C. Yang, W. Zheng, Spectrum- and time-resolved endogenous multiphoton signals reveal quantitative differentiation of premalignant and malignant gastric mucosa, Biomed. Opt. Express 9 (2018) 453–471.

[8] F. Fereidouni, Z. Harmany, M. Tian, T. Austin, K. John, M. John, B. Alexander, B. John, L. Mirna, D. Stavros, L. Richard, Microscopy with ultraviolet surface excitation for rapid slide-free histology, Nat. Biomed. Eng. 1 (2017) 957–966.

[9] O.M. Carrasco-Zevallos, C. Viehland, B. Keller, M. Draelos, A.N. Kuo, C.A. Toth, J. A. Izatt, Review of intraoperative optical coherence tomography: technology and applications [Invited], Biomed. Opt. Express 8 (2017) 1607–1637.

[10] M. Ji, D. Orringer, C. Freudiger, S. Ramkissoon, X. Liu, D. Lau, A.J. Golby, I. Norton, M. Hayashi, N. Agar, G. Young, C. Spino, S. Santagata, S. Camelo-Piragua, K. Ligon, O. Sagher, S. Xie, Rapid, label-free detection of brain tumors with stimulated Raman scattering microscopy, Sci. Transl. Med. 5 (2013) 201ra119.

[11] L. Lin, L.V. Wang, The emerging role of photoacoustic imaging in clinical oncology, Nat. Rev. Clin. Oncol. 19 (2022) 365–384.

[12] P. Beard, Biomedical photoacoustic imaging, Interface Focus 1 (2011) 602–631.

[13] T. Wong, R. Zhang, P. Hai, C. Zhang, M.A. Pleitez, R.L. Aft, D.V. Novack, L. V. Wang, Fast label-free multilayered histology-like imaging of human breast cancer by photoacoustic microscopy, Sci. Adv. 3 (2017), e1602168.

[14] S. Abbasi, D. Dinakaran, G. Bigras, J.R. Mackey, P.H. Reza, All-optical label-free human breast tissue block histology using photoacoustic remote sensing, Opt. Lett. 45 (2020) 4770–4773.

[15] J. Baik, H. Kim, M. Son, J. Choi, K.G. Kim, J. Baek, Y. Park, J. An, H.Y. Choi, S. Ryu, Y. Kim, K. Byun, C. Kim, Intraoperative label-free photoacoustic histopathology of clinical specimens, Laser Photonics Rev. 15 (2021) 2100124.

[16] T. Wong, R. Zhang, C. Zhang, H. Hsu, K.I. Maslov, L. Wang, J. Shi, R. Chen, K. K. Shung, Q. Zhou, L.V. Wang, Label-free automated three-dimensional imaging of whole organs by microtomy-assisted photoacoustic microscopy, Nat. Commun. 8 (2017) 1386.

[17] R. Cao, S.D. Nelson, S. Davis, Y. Liang, Y. Luo, Y. Zhang, B. Crawford, L.V. Wang, Label-free photoacoustic histology for intraoperative diagnosis of bone, Nat. Biomed. Eng. 7 (2023) 124–134.

[18] J. Yang, L. Gong, X. Xu, P. Hai, Y. Shen, Y. Suzuki, L.V. Wang, Motionless volumetric photoacoustic microscopy with spatially invariant resolution, Nat. Commun. 8 (2017) 780.

[19] W. Song, Y. Wu, Y. Gao, T. Chen, W. Zheng, H. Fang, L. Song, X. Yuan, Flexibly adjustable depth-of-focus photoacoustic microscopy with spatial light modulation, Appl. Phys. Lett. 113 (2018), 163502.

[20] C. Maurer, A. Jesacher, S. Bernet, M. Ritsch-Marte, What spatial light modulators can do for optical microscopy, Laser Photonics Rev. 5 (2011) 81–101.

[21] K. Lee, J. Rolland, Bessel beam spectral-domain high-resolution optical coherence tomography with micro-optic axicon providing extended focusing range, Opt. Lett. 33 (2008) 1696–1698.

[22] B. Jiang, X. Yang, Q. Luo, Reflection-mode Bessel-beam photoacoustic microscopy for in vivo imaging of cerebral capillaries, Opt. Express 24 (2016) 20167–20176.

[23] B. Park, B. Lee, H. Jeon, J. Ahn, H. Kim, C. Kim, Reflection-mode switchable subwavelength Bessel-beam and Gaussian-beam photoacoustic microscopy in vivo, J. Biophotonics 12 (2019), e201800215.

[24] N. Yu, F. Capasso, Flat optics with designer metasurfaces, Nat. Mater 13 (2014) 139–150.

[25] A. Arbabi, Y. Horie, M. Bagheri, A. Faraon, Dielectric metasurfaces for complete control of phase and polarization with subwavelength spatial resolution and high transmission, Nat. Nanotechnol. 10 (2015) 937–943.

[26] S. Jahani, Z. Jacob, All-dielectric metamaterials, Nat. Nanotechnol. 11 (2016) 23–36.

[27] H. Pahlevaninezhad, M. Khorasaninejad, Y. Huang, Z. Shi, L.P. Hariri, D.C. Adams, V. Ding, A. Zhu, C. Qiu, F. Capasso, M.J. Suter, Nano-optic endoscope for high-resolution optical coherence tomography in vivo, Nat. Photon 12 (2018) 540–547.

[28] C. Zhang, S. Divitt, Q. Fan, W. Zhu, A. Agrawal, Y. Lu, T. Xu, H.J. Lezec, Low-loss metasurface optics down to the deep ultraviolet region, Light Sci. Appl. 9 (2020) 55.

[29] L. Guo, Z. Hu, R. Wan, L. Long, T. Li, J. Yan, Y. Lin, L. Zhang, W. Zhu, L. Wang, Design of aluminum nitride metalens for broadband ultraviolet incidence routing, Nanophotonics 8 (2018) 171–180.

[30] Z. Hu, L. Long, R. Wan, C. Zhang, L. Zhang, J. Yan, H. Duan, L. Wang, Ultrawide bandgap AlN metasurfaces for ultraviolet focusing and routing, Opt. Lett. 45 (2020) 3466–3469.

[31] A.P. Konijnenberg, L. Wei, N. Kumar, L.C. Filho, L. Cisotto, S.F. Pereira, H. P. Urbach, Demonstration of an optimised focal field with long focal depth and high transmission obtained with the Extended Nijboer-Zernike theory, Opt. Express 22 (2014) 311–324.

[32] J. Braat, A. Janssen, P. Dirksen, S. van Haver, Assessment of optical systems by means of point-spread functions, Prog. Opt. 51 (2009) 349–468.

[33] S. Haver, A. Janssen, Advanced analytic treatment and efficient computation of the diffraction integrals in the extended Nijboer-Zernike, Theory, J. Eur. Opt. Soc. Rap. Publ. 8 (2013) 13044.

[34] N. Anscombe, Direct laser writing, Nat. Photon 4 (2010) 22–23.

[35] H. Li, B. Dong, X. Zhang, X. Shu, X. Chen, R. Hai, D.A. Czaplewski, H.F. Zhang, C. Sun, Disposable ultrasound-sensing chronic cranial window by soft nanoimprinting lithography, Nat. Commun. 10 (2019) 4277.

[36] W. Song, Y. Wang, H. Chen, X. Li, L. Zhou, C. Min, S. Zhu, X. Yuan, Label-free identification of human glioma xenograft of mouse brain with quantitative ultraviolet photoacoustic histology imaging, J. Biophotonics 15 (2022), e202100329.

[37] Q. Zhou, S. Lau, D. Wu, K.K. Shung, Piezoelectric films for high frequency ultrasonic transducers in biomedical applications, Prog. Mater. Sci. 56 (2011) 139–174.

[38] D. Yao, R. Chen, K. Maslov, Q. Zhou, L.V. Wang, Optimal ultraviolet wavelength for in vivo photoacoustic imaging of cell nuclei, J. Biomed. Opt. 17 (2012), 056004.

[39] Z. Wang, A.C. Bovik, H.R. Sheikh, E.P. Simoncelli, Image quality assessment: from error visibility to structural similarity, IEEE T Image Process 13 (2004) 600–612.

[40] R. Cao, J. Zhao, L. Li, L. Du, Y. Zhang, Y. Luo, L. Jiang, S. Davis, Q. Zhou, A. Zerda, L.V. Wang, Optical-resolution photoacoustic microscopy with a needle-shaped beam, Nat. Photon. 17 (2023) 89–95.

[41] X. Li, L. Kang, Y. Zhang, T. Wong, High-speed label-free ultraviolet photoacoustic microscopy for histology-like imaging of unprocessed biological tissues, Opt. Lett. 45 (2020) 5401–5404.

[42] L. Li, C. Yeh, S. Hu, L. Wang, B.T. Soetikno, R. Chen, Q. Zhou, K.K. Shung, K. I. Maslov, L.V. Wang, Fully motorized optical-resolution photoacoustic microscopy, Opt. Lett. 39 (2014) 2117–2120.

[43] D. A. D. III, T. Li, M. Vu, D. Chen, J. Zhang, R. Luo, J.Yao Horstmeyer, Reconstructing undersampled photoacoustic microscopy images using deep learning, IEEE Trans. Med. Imaging 40 (2021) 562–570.

[44] T. Vu, A. DiSpirito, D. Li, Z. Wang, X. Zhu, M. Chen, L. Jiang, D. Zhang, J. Luo, Y. Zhang, Q. Zhou, R. Horstmeyer, J. Yao, Deep image prior for undersampling high-speed photoacoustic microscopy, Photoacoustics 22 (2021), 100266.

[45] R. Shnaiderman, G. Wissmeyer, O. Ülgen, Q. Mustafa, A. Chmyrov, V. Ntziachristos, A submicrometre silicon-on-insulator resonator for ultrasound detection, Nature 585 (2020) 372–378.

[46] W. Song, F. Yang, C. Min, S. Zhu, X. Yuan, Toward ultrasensitive, broadband, reflection-mode in vivo photoacoustic microscopy using a bare glass, Laser Photonics Rev. 17 (2022) 2200030.

[47] G. Wissmeyer, Looking at sound: optoacoustics with all-optical ultrasound detection, Light.: Sci. Appl. 7 (2018) 53.

Yuting Zhao is a Ph.D. candidate at College of Physics and Optoelectronic Engineering, Shenzhen University. She received Bachelor degree from Hubei Engineering University in 2017, and received M.S. degree from Shenzhen University in 2020. Her research focuses on optical field manipulation.

Ya-chao Wang received Bachelor degree from Henan Normal University in biotechnology, Master degree from East China Normal University in biomedicine and Ph.D. degree in University of Duisburg-Essen in biology, Germany. Thereafter, he was a postdoctoral research fellow in Duke University, United States. He joined the Institute Translational Medicine, The First Affiliated Hospital of Shenzhen University (Shenzhen Second People's Hospital) in 2019. He focused on ischemic stroke, Alzheimer's disease and glioma.

Siwei Zhu received his M.M. degree from Tianjin Medical University in 1989. He works as a chief physician in Tianjin Union Medical Center, and an adjunct professor in Nankai University. His research interests include biomedicine and nanophotonics. He has published over 70 journal papers in optics and photonics.

Wei Song received his Ph.D. degree from Harbin Institute of Technology, Harbin, China, in 2014. He was an assistant professor with Shenzhen Institute of Advanced Technology from 2015 to 2016. Since 2017, he works as an assistant professor at Nanophotonics Research Centre, Shenzhen University. His main interest is the development and application of novel optical sensing and imaging technologies, including optical surface wave sensing, photoacoustic microscopy, and multimodal imaging.

Changkui Guo is a master student at the Institute of Microscale Optoelectronics, Shenzhen University. He received bachelor degree from the Changsha University in 2021. His research focuses on photoacoustic imaging.

Changjun Min received his B.S. degree and Ph.D. degree from University of Science and Technology of China in 2003 and 2008, respectively. During 2008–2011 he was a postdoctoral research fellow in Louisiana State University (USA) and then in Nanyang Technological University (Singapore). During 2011–2014, he worked as Associate Professor in Nankai University (China). Since June 2014, he joined the College of Optoelectronic Engineering in Shenzhen University (China). His research interests include plasmonics, optical sensing/imaging, optical tweezers, vector beams, and metasurface. He has published over 100 journal papers in optics and photonics.

X.-C. Yuan received B.Eng. and M.Eng. degrees in Optical Engineering from Tianjin University, China, in 1985 and 1988, respectively, and Ph.D. degree in Physics from the University of London, King's College, in 1994. Between 1994 and 1999, he was a research fellow with the Cavendish Laboratory, the University of Cambridge. Between 1999 and 2008, he was a faculty (tenured) in the School of EEE of Nanyang Technological University, Singapore. He joined the Institute of Modern Optics of Nankai University as a Chang Jiang distinguished professor in 2008. He relocated to Shenzhen University in 2013 to found the Nanophotonics Research Centre. His current work deals with optical vortices and applications, optical trapping, plasmonics in microscopy, and optical communication with orbital angular momentum. He has published more than 260 journal papers in optics and photonics. He is a SPIE and OSA Fellow.